scientific reports

Check for updates

OPEN

Variations in stiffness and structure of the human aorta along its length

Ramin Shahbad, Madihah Kazim, Sayed Ahmadreza Razian, Anastasia Desyatova & Majid Jadidi✉

This study investigates the regional mechanical, structural, and morphological properties of the human aorta using fresh tissues from 10 middle-aged and elderly donors (62 ± 11 years old, 30% female). Four locations were analyzed: descending thoracic aorta (TA), supraceliac aorta (SC), infrarenal aorta (IFR), and distal abdominal aorta (dAA). Planar biaxial testing revealed location-specific stiffness, with distal regions exhibiting significantly reduced stretch at physiological stress levels. At 75 kPa, the circumferential stretch decreased from 1.24 in the TA to 1.12 in the dAA, while longitudinal stretch declined from 1.18 to 1.12. Elastin density in the medial layer showed a marked reduction, decreasing from 23.5% in the TA to 8.9% in the dAA, accompanied by thinning and fragmentation of elastic lamellae distally. Glycosaminoglycans were primarily localized near the intima and exhibited a consistent density (~ 5–6%) across all locations. Morphometric analysis revealed a progressive decrease in wall thickness in load-free conditions from 3.10 mm in the TA to 2.77 mm in the dAA, while stress-free configurations highlighted greater residual stresses in distal segments. Constitutive modeling using four common constitutive relations, including a four-fiber family model, provided parameters for computational simulations, with the four-fiber model offering the best fit. These findings provide quantitative insights into location-specific variations in the human aorta, advancing our understanding of its biomechanical and structural heterogeneity and informing computational models and therapeutic approaches.

Keywords Aorta biomechanics, Regional aortic stiffness, Vascular mechanics, Human artery, Aorta along the length

The aorta is the largest artery in the human body, originating as the ascending thoracic aorta from the heart and gradually tapering down to the abdominal aorta and finally the common iliac arteries. This major vessel is responsible for transporting oxygenated blood from the heart to the systemic circulation and serves as a crucial buffer between the left ventricle and the peripheral vasculature. During systole, the aorta absorbs the non-continuous blood flow ejected from the left ventricle, expanding to store elastic energy. This stored energy is then released during diastole, creating a nearly continuous blood flow to the peripheral tissues[1]. This dynamic function, commonly known as the Windkessel effect, plays an essential role in maintaining steady blood flow and regulating systemic blood pressure[2]. Increased aortic stiffness and reduced elasticity often lead to impairment of the Windkessel function, which is associated with elevated cardiovascular risks, including hypertension, diabetes, hyperlipidemia, and atherosclerosis[2–4]. This functional decline can arise from various alterations in the aorta, with the most critical being changes in the aorta's mechanical responses to pulsatile loading, structural modifications in the arterial wall, and morphological adaptations[5]. These alterations collectively compromise the aorta's ability to buffer and maintain hemodynamic stability. Given the significance of this issue, the mechanical, structural, and morphological characteristics of the aorta have been extensively investigated in both ex-vivo and in-vivo studies, enhancing our understanding of aortic health and disease.

Location-specific studies of the aorta have garnered significant interest due to the regional variability in disease progression and development, such as atherosclerosis, dissection, and aneurysms[6–8]. For instance, aortic dissection is more commonly observed in the thoracic region[9], whereas aneurysms are frequently seen in the abdominal segment, with each area exhibiting distinct underlying mechanisms of disease progression[10]. Additionally, regional differences in aortic characteristics are essential in designing grafts and medical devices, as biomechanical compatibility with native aortic tissue is critical to device effectiveness and longevity[11–13]. Therefore, understanding these location-dependent variations is important for advancing aortic disease research and optimizing the design of aortic repair devices.

To date, several in-vivo[14–19] and ex-vivo[7,8,11,12,20–27] studies have quantified aortic properties at specific locations along the vessel. In-vivo studies, however, are limited in their ability to examine the detailed wall

Department of Biomechanics, University of Nebraska Omaha, Omaha, NE, USA. ✉email: mjadidi@unomaha.edu

structure and intrinsic mechanical properties of the aorta. These studies are typically restricted to investigating anatomical dimensions and flow-related measurements, which can be indirectly linked to the aorta's mechanical behavior. Pulse wave velocity (PWV) and distensibility are two primary indices widely used as markers of aortic stiffness[16,18,28]. Over the last few decades, advancements in computed tomography (CT) and magnetic resonance imaging (MRI) have enabled more accurate and controlled measurements of aortic dimensions and flow characteristics across different segments, offering deeper insights into segmental variability in aortic mechanical behavior[18,28,29]. For instance, distensibility and segmental PWV have been extensively measured at various aortic locations, including the arch[16,30], ascending thoracic[14–16], different segments of the descending thoracic[14–18], and abdominal regions[14,15,17]. These measurements have provided valuable data across different ages, sexes, and diseased cohorts, revealing trends in aortic stiffness associated with age[14,19], and physiological and pathological variability[16,18]. To examine the intrinsic mechanical properties of the aorta—characteristics that are challenging to capture in-vivo—ex-vivo studies are essential. Several ex-vivo studies have employed a range of mechanical testing methods to analyze regional variation along the aorta. Common approaches include uniaxial[12,21], planar biaxial[8,11,23–25], and inflation-extension[22,27] tests, each designed to characterize segmental stiffening in detail. Additionally, full-field measurement techniques like digital image correlation (DIC) and speckle tracking have captured spatial strain variations and local mechanical behavior, offering high-resolution insights into aortic wall deformation and anisotropy. These studies revealed the complex heterogeneity of aortic mechanics and underscore the need for refined models to account for regional strain differences[31–34]. Ex-vivo studies also allow for detailed examination of wall extracellular matrix (ECM) across different aortic locations, utilizing histological or multiphoton imaging to assess the tissue's structural and compositional variability[8,11,21].

Among the ex-vivo studies focused on location-dependent aortic properties, Guo and Kassab[7] were among the earliest to explore the variation in mice aortic mechanics, measuring opening angles, stretch ratios, and stress distributions along five thoracic and abdominal locations. Similarly, Lillie and Gosline[20] examined location-specific stiffness along the porcine descending thoracic aorta using ring tests, while Sokolis[21] expanded on this approach by assessing circumferential stiffening and structural changes across nine porcine thoracic and abdominal sites through uniaxial and histological analyses. Haskett et al.[8] conducted one of the most comprehensive studies, revealing the relationship between aging, structural organization, and mechanical behavior of the human aorta. Their study spanned a wide age range and included analysis at five anatomical locations, from the ascending aorta to the abdominal aorta, using advanced techniques such as small-angle light scattering and multiphoton microscopy. Kim et al.[22] applied inflation-extension testing to measure circumferential stretch and stress differences between proximal and distal segments of the porcine descending thoracic aorta. Azadani et al.[23] and Kamenskiy et al.[11] compared mechanical and structural properties of the middle-aged human ascending aorta, aortic sinuses, and thoracic vs. abdominal segments through biaxial testing, highlighting implications for improving medical device developments. Zeinali-Davarani et al.[24] studied the porcine aorta's structural and mechanical variation across four thoracic segments using biaxial testing, while Peña et al.[12,25] measured wall layers stiffness, residual stresses, and geometric differences, focusing specifically on proximal vs. distal regions of the porcine thoracic aorta. More recently, Sokolis et al.[26] examined anatomical features and axial prestretch from the aortic root to the iliac bifurcation in the human aorta, and Dwivedi et al.[27] combined inflation-extension testing with fluorescence imaging across three segments of porcine aorta to correlate residual stresses and mechanical responses with quantitative structural components.

Together, these studies have significantly advanced our understanding of the aorta's structural and mechanical heterogeneity along its length, highlighting the importance of regional variations in both physiological and pathological contexts. Findings consistently demonstrate a gradual increase in stiffness with increasing distance from the heart, as evidenced by reductions in aortic distensibility, increases in PWV, and variations in intrinsic mechanical properties and residual stresses. These changes are closely associated with geometric adaptations[35], alterations in microstructural organization[36], and the heterogeneous flow dynamics across different segments of the aorta[37]. Collectively, these insights emphasize that the aorta's biomechanical and structural properties are not uniform but instead tailored to meet the unique functional demands of each anatomical region. However, several limitations remain. First, these studies often focus on comparisons between only two locations, limiting a broader understanding of location-dependent variations across the entire aortic length. Second, most studies do not examine mechanical, structural, and morphometric characteristics from the same subject, which is crucial for an integrated analysis of the aortic wall. Lastly and most significantly, many studies rely on animal models such as porcine[12,20,21,24,25,27] or murine[7] aortas rather than human tissue. Although animal models contribute to our understanding of basic physiological mechanisms, they do not entirely capture human-specific vascular properties due to differences in factors like heart rate, vascular structure, immune response, and lifespan[38]. For example, elastin, a key protein contributing to arterial elasticity, undergoes degradation and fragmentation with age in humans, leading to a stiffer arterial wall—a phenomenon less observed in animals because of their shorter lifespans[39].

In this study, we aimed to address these limitations by comprehensively examining the mechanical, morphometric, and structural properties along the human aorta. Using fresh human aortas from donors, we analyzed clinically relevant locations along the aorta with planar biaxial testing and detailed bi-directional histology. This approach allowed for a thorough assessment of the aortic wall's characteristics at multiple locations within each subject. Moreover, we provided parameters for established constitutive models, offering a foundation for computational studies focused on aortic biomechanics. The findings contribute to our understanding of human aortic physiology and pathophysiology and may inform the design of biomimetic materials and devices tailored for site-specific vascular repair.

Methods

Aorta specimens collection and preparation

40 specimens were collected from 10 aortas obtained from middle-aged and older deceased human donors (62 ± 11 years old, range 39–76 years, 30% female), provided by an organ procurement organization, Live On Nebraska. Age and sex (Male: M, Female: F) of subjects include S1: 76 F, S2: 75 M, S3: 57 M, S4: 68 M, S5: 60 F, S6: 68 M, S7: 67 M, S8: 39 F, S9: 63 M, and S10: 51 M. The aortas were excised within 24 h post-mortem after obtaining informed consent from the next of kin. The excised aortas spanned from the descending thoracic aorta, just distal to the right subclavian artery, to the distal abdominal aorta, immediately proximal to the aorto-iliac bifurcation. Upon excision, the aortas were immediately transported to our laboratory in 0.9% phosphate-buffered saline (PBS) at 4 °C to maintain tissue viability. All specimens were tested on the same day to preserve their mechanical integrity and biological properties. Before testing, the aortas were carefully cleaned of loose surrounding tissue (Fig. 1A).

To investigate regional differences in mechanical, structural, and morphometric properties along the length of the aorta, four tissue specimens were collected from predefined anatomical locations: (1) descending thoracic aorta (TA), 1 cm distal to the left subclavian artery, (2) supraceliac aorta (SC), right above the celiac trunk, (3) infrarenal aorta (IFR), 1 cm below the renal arteries, and (4) distal abdominal aorta (dAA), right above the aortoiliac bifurcation, resulting in a total of 40 tissue specimens. Each tissue specimen was prepared for three types of analyses: morphometric measurements, mechanical, and structural characterization. To accommodate these analyses, each specimen was segmented into two thin rings (~1 mm thick) and one 13 mm × 13 mm segment, as illustrated in Fig. 1B. The rings were used for morphometric and structural analysis (Fig. 1C and E), while the 13 mm × 13 mm segment was reserved for biaxial mechanical testing. The excised samples were placed in a petri dish filled with PBS at room temperature, allowing the samples to float freely and ensuring that they remained hydrated and undistorted during the tests. Care was taken to maintain consistency in the orientation of the samples to ensure reproducibility of the mechanical and structural measurements.

Morphometric measurements

Morphometric analysis was conducted on the two rings obtained from each aortic segment. One of the rings was radially cut from the posterolateral region to release the circumferential residual stresses, allowing it to be measured in a stress-free condition (cut-ring)[40]. The uncut ring served as the load-free sample. Both rings and cut-rings stayed in PBS solution for 30 min at room temperature prior to imaging to ensure hydration and stabilization of their physical properties. The samples were photographed, and the resulting images were analyzed using custom-written image-processing software developed in Visual Studio C# with the .Net 4.8 framework[41] (Fig. 1C). The intimal and adventitial lengths (L_{int} and L_{adv}) were measured from the stress-free cut-ring by tracing the inner and outer arcs of the sample. The wall thickness was determined by selecting a series of

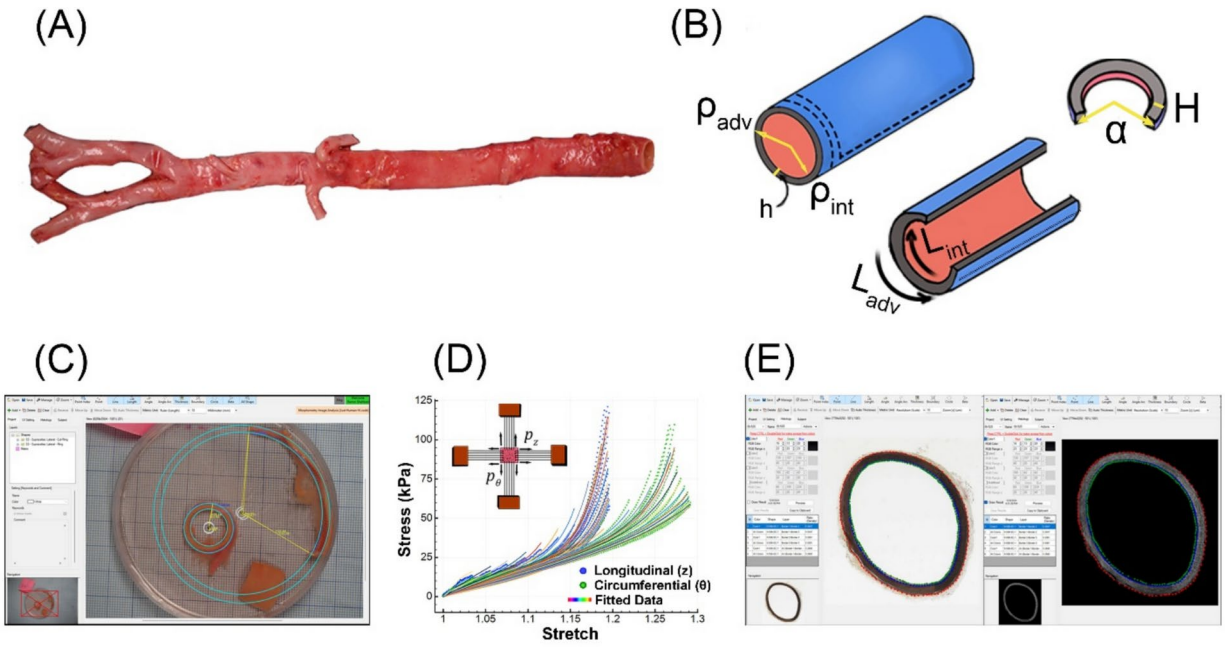

Fig. 1. Overview of the experimental methodology. (**A**) Harvested human aorta, carefully cleaned of surrounding loose tissue. (**B**) Arterial specimens excised from each aortic location, cut into a 13 × 13 mm segment, and stress-free cut-ring, illustrating key morphometric parameters. (**C**) Morphometric analysis of rings and cut-ring samples using custom image-processing software. (**D**) Representative biaxial stress-stretch curves showing nonlinear anisotropic behavior in longitudinal and circumferential directions with model-fitted data. (**E**) Histological analysis of load-free ring samples stained with Movat's Pentachrome, highlighting segmentation and density quantification of structural components of the aortic wall.

equally spaced points on both the intimal and adventitial surfaces in both the load-free (h) and stress-free (H) samples. The software computed the distances between these points, providing the average wall thickness. In addition, best-fitting circles were fitted to the intimal and adventitial layers of both the stress-free and load-free samples. The angle between the starting and ending points of the circles, relative to the circle's center, was then calculated to determine the opening angle (α) from the stress-free cut-ring. For the load-free ring, the fitted circles on the intimal and adventitial surfaces were used to estimate the intimal and adventitial radii (ρ_{int} and ρ_{adv}). These measurements provided detailed geometric characterization of the aortic wall under both load-free and stress-free conditions.

Mechanical characterization

Planar biaxial tests were performed on a 13 mm × 13 mm stress-free specimen excised from the lateral side of each aortic segments to determine the intrinsic mechanical behavior of the arterial tissue. The tests were conducted using a CellScale Biotester equipped with 2.5 N load cells while the samples were immersed in 0.9% PBS solution at 37 °C. The longitudinal and circumferential directions of the tissue were aligned with the x- and y-axes of the biaxial testing machine, respectively. The samples were attached using rakes, as shown in Fig. 1D. Graphite particles were sprinkled on the specimen surfaces to track deformations in the central region, minimizing edge effects near the rakes. The biaxial testing protocol consisted of three main steps: maximum stretch estimation, preconditioning, and the primary test. In the first step, tissues were subjected to multi-level loading and unloading, ranging from 200 to 2200 mN, applied equibiaxially to estimate the maximum stretch in the longitudinal ($\lambda_z^{\max}$) and circumferential ($\lambda_\theta^{\max}$) directions. Subsequently, during preconditioning, the tissues were stretched equibiaxially to these maximum stretches through ten loading and unloading cycles to establish a repeatable pseudoelastic response. In the final step, tissues were subjected to 21 multi-ratio stretch-controlled protocols to gather sufficient data for constitutive modeling. These protocols ranged from circumferential (λ_θ) to longitudinal (λ_z) stretch ratios of $\lambda_\theta : \lambda_z = \lambda_\theta^{\max} : (1 + ((\lambda_z^{\max} - 1) \times 10\%))$ to $\lambda_\theta^{\max} : (1 + ((\lambda_z^{\max} - 1) \times 90\%))$ and $\lambda_\theta : \lambda_z = (1 + ((\lambda_\theta^{\max} - 1) \times 90\%)) : \lambda_z^{\max}$ to $(1 + ((\lambda_\theta^{\max} - 1) \times 10\%)) : \lambda_z^{\max}$ with steps of 10%. Three equibiaxial protocols, i.e., $\lambda_\theta : \lambda_z = \lambda_\theta^{\max} : \lambda_z^{\max}$ were interspersed at the beginning, middle, and end of the sequence to monitor for tissue damage. All specimens were tested at the strain rate of $0.01s^{-1}$. Assuming incompressibility, the experimental Cauchy stresses in the circumferential ($T_{\theta\theta}^{\exp}$) and longitudinal ($T_{zz}^{\exp}$) directions were calculated as:

$$T_{\theta\theta}^{\exp} = \lambda_\theta \frac{p_\theta}{HL_z}; T_{zz}^{\exp} = \lambda_z \frac{p_z}{HL_\theta}, \tag{1}$$

where p_θ and p_z are the applied circumferential and longitudinal loads, respectively, H is the stress-free thickness of the mechanically tested specimen, and L_θ and L_z are the initial dimensions of the specimen in the circumferential and longitudinal directions, respectively.

Constitutive modeling

To describe the mechanical response of the aortic tissues under planar biaxial deformation, four commonly used constitutive models were fitted to the experimental data. These models included the neo-Hookean, Demiray-Delfino, two-fiber family Holzapfel-Gasser-Ogden (HGO), and four-fiber family models. Each model provided a framework for characterizing the stress–strain behavior in both the circumferential and longitudinal directions under biaxial loading conditions. The circumferential and longitudinal stresses for each model in planar biaxial deformation were calculated using the following Eqs. 44:

Neo-Hookean:

$$T_{\theta\theta} = \mu \left(\lambda_\theta^2 - \frac{1}{\lambda_z^2 \lambda_\theta^2} \right), T_{zz} = \mu \left(\lambda_z^2 - \frac{1}{\lambda_z^2 \lambda_\theta^2} \right), \tag{2}$$

where μ is the material parameter.

Demiray-Delfino:

$$T_{\theta\theta} = D_1 \left(\exp \left[\frac{D_2}{2} (I_{\mathbf{C}} - 3) \right] \right) \left(\lambda_\theta^2 - \frac{1}{\lambda_z^2 \lambda_\theta^2} \right), \tag{3}$$

$$T_{zz} = D_1 \left(\exp \left[\frac{D_2}{2} (I_{\mathbf{C}} - 3) \right] \right) \left(\lambda_z^2 - \frac{1}{\lambda_z^2 \lambda_\theta^2} \right), \tag{4}$$

where D_1 and D_2 are the material parameters and $I_{\mathbf{C}} = \lambda_\theta^2 + \lambda_z^2 + \frac{1}{\lambda_\theta^2 \lambda_z^2}$.

Two-fiber family HGO:

$$T_{\theta\theta} = c_{gr} \left(\lambda_\theta^2 - \frac{1}{\lambda_z^2 \lambda_\theta^2} \right) + \sum_{i=1}^{2} 2c_1^i I V_C^i - 1 e^{c_2^i \left(I V_C^i - 1 \right)^2} \lambda_\theta^2 \sin^2 \gamma, \tag{5}$$

$$T_{zz} = c_{gr} \left(\lambda_z^2 - \frac{1}{\lambda_z^2 \lambda_\theta^2} \right) + \sum_{i=1}^{2} 2c_1^i I V_{\mathbf{C}}^i - 1 e^{c_2^i \left(I V_{\mathbf{C}}^i - 1 \right)^2} \lambda_z^2 cos^2 \gamma, \tag{6}$$

where $c_{gr}, c_1^1 = c_1^2 = c_1, c_2^1 = c_2^2 = c_2$, and$\gamma$ are the material parameters and $IV_{\mathbf{C}}^{1,2} = \lambda_z^2 cos^2\gamma + \lambda_\theta^2 sin^2\gamma$.

Four-fiber family:

$$T_{\theta\theta} = c_{gr}\left(\lambda_\theta^2 - \frac{1}{\lambda_z^2\lambda_\theta^2}\right) + c_1^3\lambda_\theta^2 - 1e^{c_2^3\left(\lambda_\theta^2-1\right)^2}\lambda_\theta^2 + \sum_{i=1}^{2} c_1^i IV_{\mathbf{C}}^i - 1e^{c_2^i\left(IV_{\mathbf{C}}^i-1\right)^2}\lambda_\theta^2 sin^2\gamma, \tag{7}$$

$$T_{zz} = c_{gr}\left(\lambda_z^2 - \frac{1}{\lambda_z^2\lambda_\theta^2}\right) + c_1^4\lambda_z^2 - 1e^{c_2^4\left(\lambda_z^2-1\right)^2}\lambda_z^2 + \sum_{i=1}^{2} c_1^i IV_{\mathbf{C}}^i - 1e^{c_2^i\left(IV_{\mathbf{C}}^i-1\right)^2}\lambda_z^2 cos^2\gamma, \tag{8}$$

where $c_{gr}, c_1^1 = c_1^2, c_2^1 = c_2^2, c_1^3, c_2^3, c_1^4, c_2^4, \gamma$ are the material parameters, and $IV_C^{1,2} = \lambda_z^2 \cos^2\gamma + \lambda_\theta^2 \sin^2\gamma$. Macaulay brackets $\langle(\cdot)\rangle = \frac{1}{2}\left[(\cdot) + |(\cdot)|\right]$ are used in two- and four-fiber family models to filter positive values so fibers only contribute to stress during tension.

Material parameters for each constitutive model were determined by minimizing the error between the experimental and theoretical stresses calculated from the models. This was achieved using the differential evolution algorithm[43]. Differential evolution operates by iteratively improving candidate solutions with respect to a given measure of quality—here, the error between experimental and predicted stresses—by combining and mutating potential solutions over successive generations, ultimately converging on the optimal set of material parameters. The quality of the fits to the experimental data was assessed using the root mean squared error (RMSE) to quantify the average discrepancy between experimental and predicted stresses and the coefficient of determination (R^2) to assess the goodness of fit (Fig. 1D).

Structural analysis

The structural analysis of the aortic samples was conducted through histological examination to assess the composition and organization of the ECM. This analysis was performed on the load-free ring samples previously used for morphometric measurements. Following the imaging for morphometry, the samples were fixed in methacarn, dehydrated in 70% ethanol, embedded in paraffin, and sectioned using a microtome. The histological sections were stained with Movat's Pentachrome to quantify key ECM components, including elastin and glycosaminoglycans (GAGs) (Fig. 1E). The stained slides were scanned using a Leica Aperio CS2 scanner at 20× magnification. The scanned images, initially in SVS file format, were converted to JPEG format using custom-developed Histology Image Viewer and Converter software[44].

The converted images were analyzed semi-automatically using a custom-written software application developed in Visual Studio C# with the .Net 4.8 framework and OpenCV libraries[5,41]. The analysis began with the manual selection of three lines along the arterial wall boundaries: one along the lumen surface, one at the interface between the tunica intima and tunica media, and one at the outer edge of the tunica media. This approach ensured precise delineation of the layers for further analysis. RGB color thresholding was then applied to quantify the density of specific intramural constituents. Separate color thresholds were set for elastin and GAGs, allowing their densities to be quantified as the percentage of pixels with the assigned color relative to the total area of the analyzed region. All analyses were performed twice by a single operator to minimize measurement error, and the results were averaged.

Statistical analysis

Statistical analysis was performed using R in RStudio software (R for windows 4.2.1, RStudio version 2023.12.0+369, https://posit.co/download/rstudio-desktop/) to investigate potential differences in the morphological, mechanical, and structural characteristics across the four major anatomical locations: TA, SC, IFR, and dAA. The Shapiro–Wilk test was used to assess normality, and Levene's test evaluated the homogeneity of variances. Differences between groups were analyzed using t-test, one-way and two-way repeated measures (RM) ANOVAs, and their non-parametric alternative tests as appropriate with partial eta squared (η^2) reported to measure effect sizes. The Mauchly test assessed sphericity in RM ANOVAs, and the Greenhouse–Geisser (GG) correction was applied when the sphericity assumption was violated. Post-hoc pairwise comparisons were conducted using Bonferroni correction to identify specific anatomical locations with significant differences. In all analyses, a p-value of less than 0.05 was considered statistically significant.

Results

Morphological analysis

Changes in human aortic morphometry and anatomical measurements along the length from the TA to the dAA are shown in Fig. 2. An increasing trend in the opening angle was observed from TA to IFR (TA: 157.77°, SC: 183.78°, IFR: 201.93°), followed by a decrease at dAA (151.15°). However, these changes were not statistically significant ($p = 0.656$) Fig. 2A.

The intimal and adventitial radii of the aorta exhibited a decreasing trend along the length, most notably until the IFR, as shown in Fig. 2B. The ρ_{int} decreased from 9.30 mm in TA to 8.08 mm (SC), 6.53 mm (IFR), and 6.66 mm (dAA). Similarly, the ρ_{adv} decreased from 12.72 mm in TA to 11.11 mm (SC), 9.71 mm (IFR), and 9.43 mm (dAA). The results of the GG corrected test indicated significant differences between locations for both ρ_{int} ($p = 0.002$) and ρ_{adv} ($p = 0.004$). Effect size analysis suggested that location explained 68.5% of the variability in ρ_{int} and 62.1% for ρ_{adv}. Pairwise comparisons revealed significant differences between most locations, except for TA versus IFR and SC versus dAA for ρ_{int}. For ρ_{adv}, significant differences were only observed between TA versus dAA and TA versus IFR.

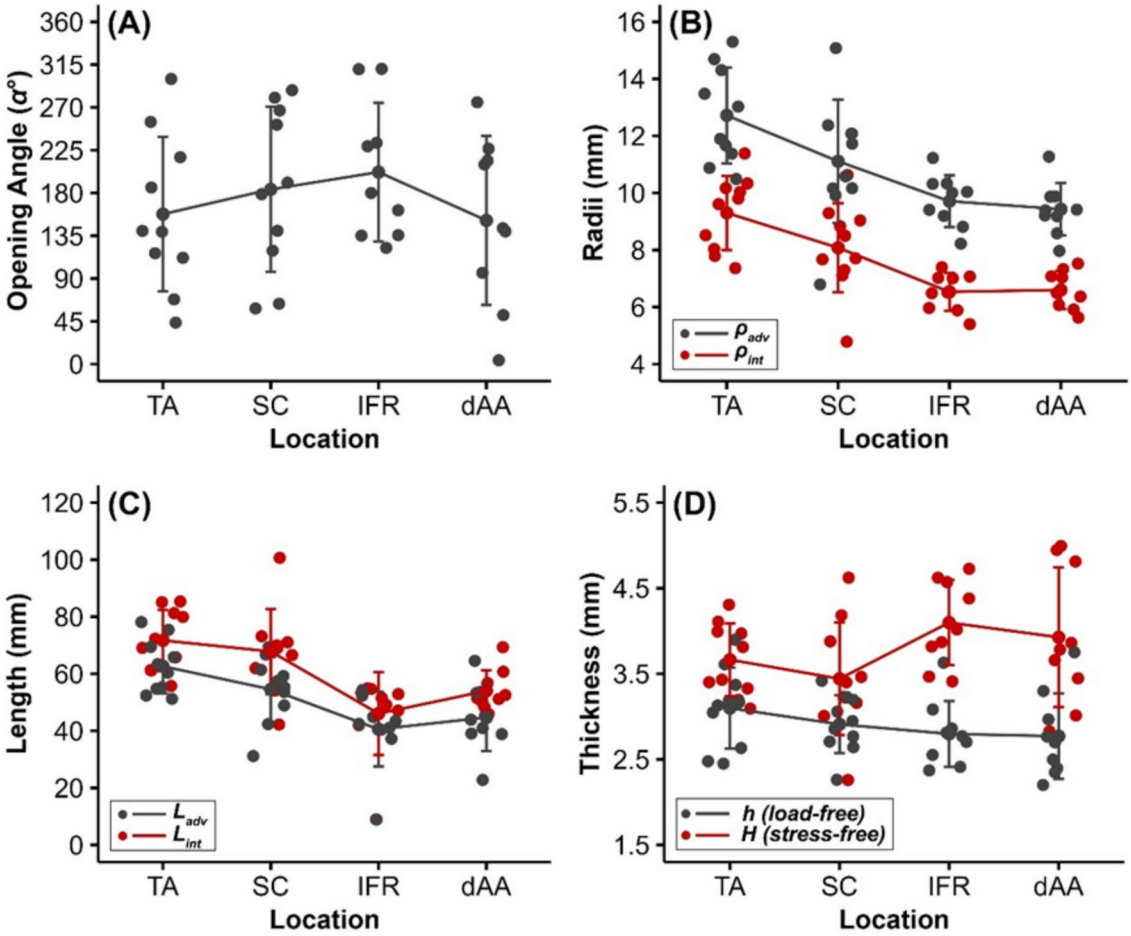

Fig. 2. The impact of location on changes in (**A**) stress-free cut ring opening angle (α), (**B**) intima and adventita radii (ρ_{int} and ρ_{adv}), (**C**) intima and adventitia length (L_{int} and L_{adv}), and (**D**) load-free ring (h) and stress-free cut ring (H) thicknesses. Each plot shows individual data points (colored dots) for each subject along with the mean ± standard deviation (solid lines with error bars).

Figure 2C shows the location dependency of intimal and adventitial stress-free cut-ring lengths. Both L_{int} and L_{adv} decreased from TA to IFR, followed by a slight increase at dAA. One-way RM ANOVA, with GG correction, revealed a significant effect of location on both L_{int} ($p = 0.004$) and L_{adv} ($p < 0.001$), with location explaining 54.3% and 52.4% of the variance, respectively. Significant differences in L_{int} were observed between TA versus dAA, TA versus IFR, and SC versus IFR, while L_{adv} differences were limited to TA versus dAA and TA versus IFR. In all locations, L_{int} was consistently 13–25% longer than L_{adv} (TA: 71.70 mm versus 62.63 mm, SC: 67.83 mm versus 54.56 mm, IFR: 46.05 mm versus 40.56 mm, and dAA: 54.01 mm vs. 44.70 mm), which can also be visually observed in Fig. S1 of Supplement, where the stress-free cut rings in IFR and dAA curve outward rather than inward in a representative subject.

The effect of location on aortic wall thickness is illustrated in Fig. 2D. To evaluate the influence of residual stress release on wall thickness, a two-way repeated-measures ANOVA was conducted with aortic location (TA, SC, IFR, dAA) and tissue condition (load-free vs. stress-free) as independent factors. The analysis revealed that wall thickness in the stress-free configuration (TA = 3.66 mm, SC = 3.44 mm, IFR = 4.10 mm, dAA = 3.93 mm) was significantly greater than in the load-free configuration (TA = 3.10 mm, SC = 2.91 mm, IFR = 2.80 mm, dAA = 2.77 mm) ($p < 0.001$), indicating that the aortic wall expands upon the release of residual stresses. While no significant differences in thickness were observed across locations in the load-free configuration, a significant location-dependent difference was found for stress-free cut-ring samples ($p = 0.034$), accounting for 30% of the thickness variation. However, pairwise comparisons did not reveal any significant differences between specific locations, likely due to the small effect size (0.3) and the conservative Bonferroni correction applied. A simple paired t-test between individual locations showed a significant difference between SC and IFR ($p = 0.018$). However, this approach should be interpreted with caution as it increases the risk of Type I errors (false positives).

Mechanical analysis

The equibiaxial stress-stretch responses of mechanically tested samples for all 10 subjects are illustrated in Fig. 3, classified by anatomical location (TA, SC, IFR, and dAA) and loading direction (longitudinal and circumferential). All mechanical responses were plotted within the same range for stress (0–85 kPa) and

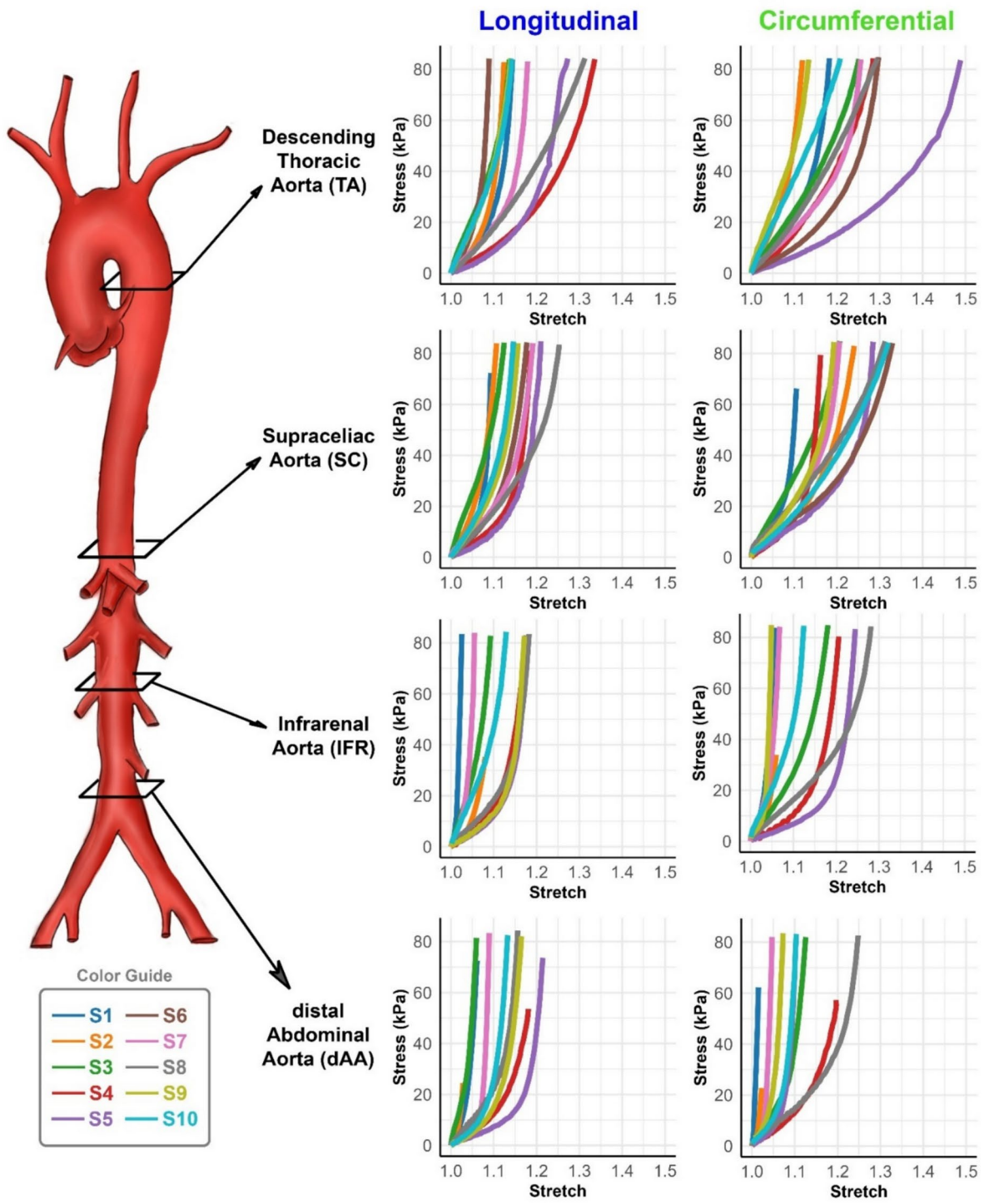

Fig. 3. Stress-stretch response curves of aortic tissue samples from ten subjects (S1–S10) across four anatomical locations: TA, SC, IFR, and dAA. Stress-stretch curves in the longitudinal and circumferential directions are shown in the left and right columns, respectively. Each line color corresponds to an individual subject, as indicated in the color guide. The curves demonstrate a progressive increase in stiffness moving distally along the aorta.

stretch (1–1.5) to facilitate location- and direction-wise comparisons. From these curves, a general decline in tissue stretch capability can be observed when moving distally from the TA to the dAA, most notably in the longitudinal direction.

The stress-stretch curves from biaxial mechanical testing were used to assess the intrinsic mechanical properties of the stress-free aortic wall specimens. To quantify intrinsic stiffness, we examined the stretch at a specific stress levels (25, 50, and 75 kPa), which serves as an indicator of tissue compliance, as well as the tangent

modulus, defined as the slope of the stress-stretch curve within these stress levels (low stress range: 25–50 kPa and high stress range: 50–75 kPa). These metrics provide a comprehensive assessment of the intrinsic material behavior of the aorta across different anatomical locations. The results and comparisons of these stiffness metrics across different anatomical locations and loading directions are presented in Fig. 4 and Table S1 of Supplement. A two-way RM ANOVA was conducted to evaluate the effects of location and direction on stretch, enabling comparison of stiffness across locations (TA, SC, IFR, dAA) and directions (longitudinal and circumferential) at different stress levels.

At 25 kPa, results indicated a marginal effect of location on stretch ($p = 0.057$), suggesting a potential trend in stiffness variation along the aortic length, though this result did not reach conventional statistical significance. No significant main effect of direction was observed ($p = 0.716$), indicating similar stiffness across longitudinal and circumferential directions at this stress level. Additionally, the interaction between location and direction was non-significant ($p = 0.364$), suggesting that any effect of location on stiffness did not depend on loading direction. At 50 kPa, the two-way RM ANOVA revealed a significant effect of location on arterial stretch ($p < 0.001$), indicating that stiffness differs significantly across anatomical locations along the aorta. However, there was no significant effect of direction on stretch ($p = 0.192$), nor a significant interaction between location and direction ($p = 0.251$), suggesting that location-specific differences in stiffness are consistent across both loading directions. Pairwise comparisons, adjusted with Bonferroni correction, confirmed significant differences in the stretch between proximal and distal locations, particularly between TA (1.177 ± 0.082) and both IFR (1.121 ± 0.062) ($p = 0.007$) and dAA (1.112 ± 0.062) ($p = 0.022$), as well as between SC (1.167 ± 0.054) and both IFR ($p = 0.036$) and dAA ($p = 0.028$). At 75 kPa, similar to the 50 kPa, results from statistical tests revealed a significant effect of location on arterial stretch ($p < 0.001$), indicating that stiffness varies significantly along the aortic length. Pairwise comparisons showed that both IFR (1.134 ± 0.076) and dAA (1.117 ± 0.058) locations are significantly stiffer than proximal locations TA (1.210 ± 0.095) and SC (1.203 ± 0.062), particularly with TA versus IFR ($p < 0.001$), TA vs. dAA ($p = 0.032$), and SC vs. dAA ($p = 0.013$) showing notable differences. In contrast, the direction did not show a significant main effect on stiffness ($p = 0.239$), nor did the direction-location interaction ($p = 0.298$), suggesting consistent location-specific differences in stiffness across both directions.

In the more proximal locations, the difference between longitudinal and circumferential directions was more pronounced than in distal locations. Specifically, SC exhibited a significant directional dependency, with $p = 0.006$ at 50 kPa and $p = 0.007$ at 75 kPa. For TA, the directional dependency approached significance, with $p = 0.116$ at 50 kPa and $p = 0.067$ at 75 kPa. No significant directional differences were observed at the more distal locations, IFR and dAA, indicating that the directional effect on stiffness and anisotropy decreases along the length of the aorta.

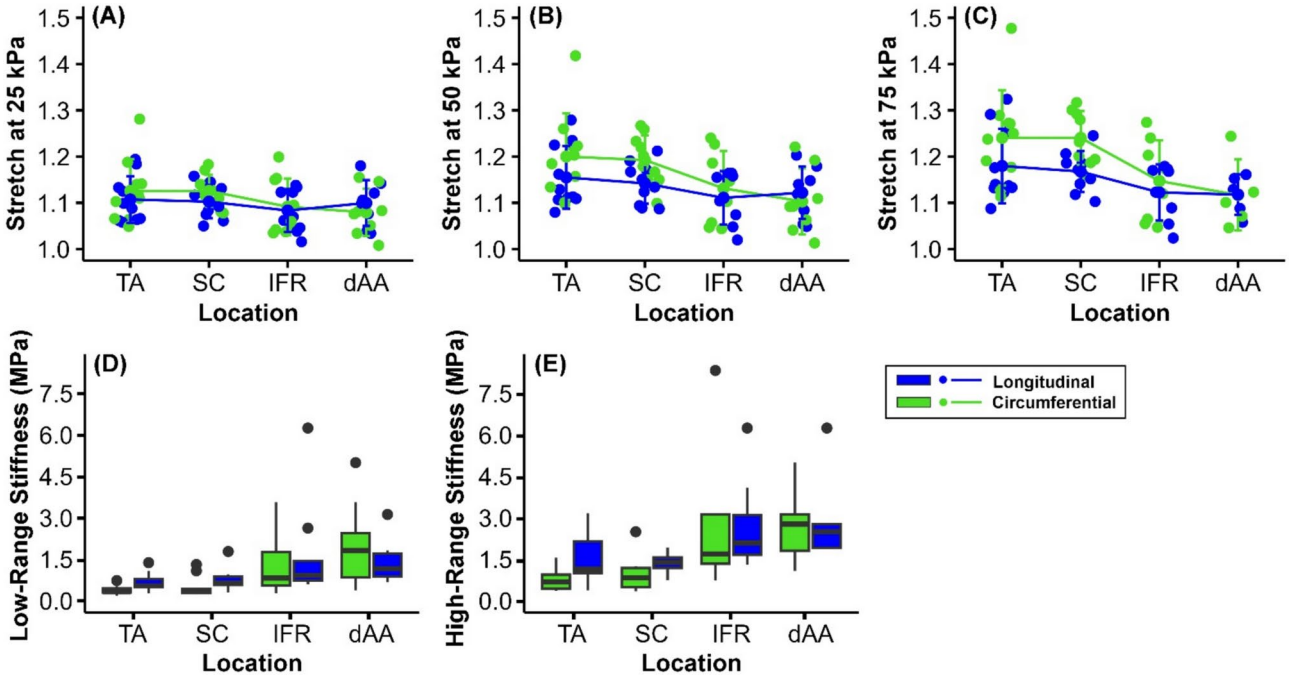

Fig. 4. Stretch values in the longitudinal (blue) and circumferential (green) directions at each anatomical location (TA, SC, IFR, and dAA) along the aorta, measured at stress levels of (**A**) 25, (**B**) 50, and (**C**) 75 kPa. Each plot shows individual data points (colored dots) for each subject along with the mean ± standard deviation (solid lines with error bars). Box plots of (**D**) low-range stiffness (linear stiffness in the 25–50 kPa range) and (**E**) high-range stiffness (linear stiffness in the 50–75 kPa range) at each aortic location. Outliers are represented as black dots. The visual trend suggests a general decline in stretch values and a general increase in linear stiffness from proximal (TA and SC) to distal locations (IFR and dAA), particularly at higher stress levels, indicating increased stiffness in distal regions.

Similar to stretch at specific stress levels, statistical analysis of linear stiffness within the 25–50 kPa range (low-range stiffness) revealed a significant dependence on location ($p = 0.011$). Stiffness was lower in proximal locations and increased distally, with dAA exhibiting significantly higher stiffness compared to both TA ($p = 0.004$) and SC ($p = 0.021$). However, these location-dependent differences were not direction-specific, as the interaction between location and loading direction was not significant ($p = 0.325$). A similar trend was observed for high-range stiffness (linear stiffness within the 50–75 MPa range). Location had a significant effect on stiffness ($p = 0.033$), while loading direction remained an independent factor ($p = 0.438$). In addition to dAA being significantly stiffer than TA ($p = 0.003$) and SC ($p = 0.011$), IFR also exhibited higher stiffness than TA under higher loading conditions ($p = 0.006$).

To provide a more detailed visual comparison, the stress-stretch curves across four locations and two directions were also plotted individually for each subject shown in Supplement (Fig. S2). In the longitudinal direction, visual comparison showed that in 60% of subjects, the TA exhibited the most compliant behavior, with the SC being the most compliant in 30% of subjects. The IFR appeared as the stiffest location in 50% of subjects, while 30% of subjects showed the dAA as the stiffest in response to mechanical loading. In the circumferential direction, the TA and SC locations consistently displayed the highest compliance across all subjects, with half of the subjects showing TA as the most compliant and the other half showing SC. The dAA location appeared as the stiffest in 70% of subjects, and in 80% of subjects, both TA and SC were more compliant than IFR and dAA. In the circumferential direction, two prominent trends of increasing stiffness with location change were seen across 70% of subjects: TA → SC → IFR → dAA and SC → TA → IFR → dAA. In all subjects following these trends, the IFR consistently exhibited greater compliance than the dAA.

Constitutive modelling

Four constitutive relations were fitted to the 19 unique biaxial protocols for all subjects at four anatomical locations. A representative fit of these four constitutive models is shown for subject S7 (67 M) TA sample in Fig. 5. The RMSE of the four-fiber family ranged from 0.551 to 18.098 kPa (3.330 ± 3.721 kPa), the two-fiber

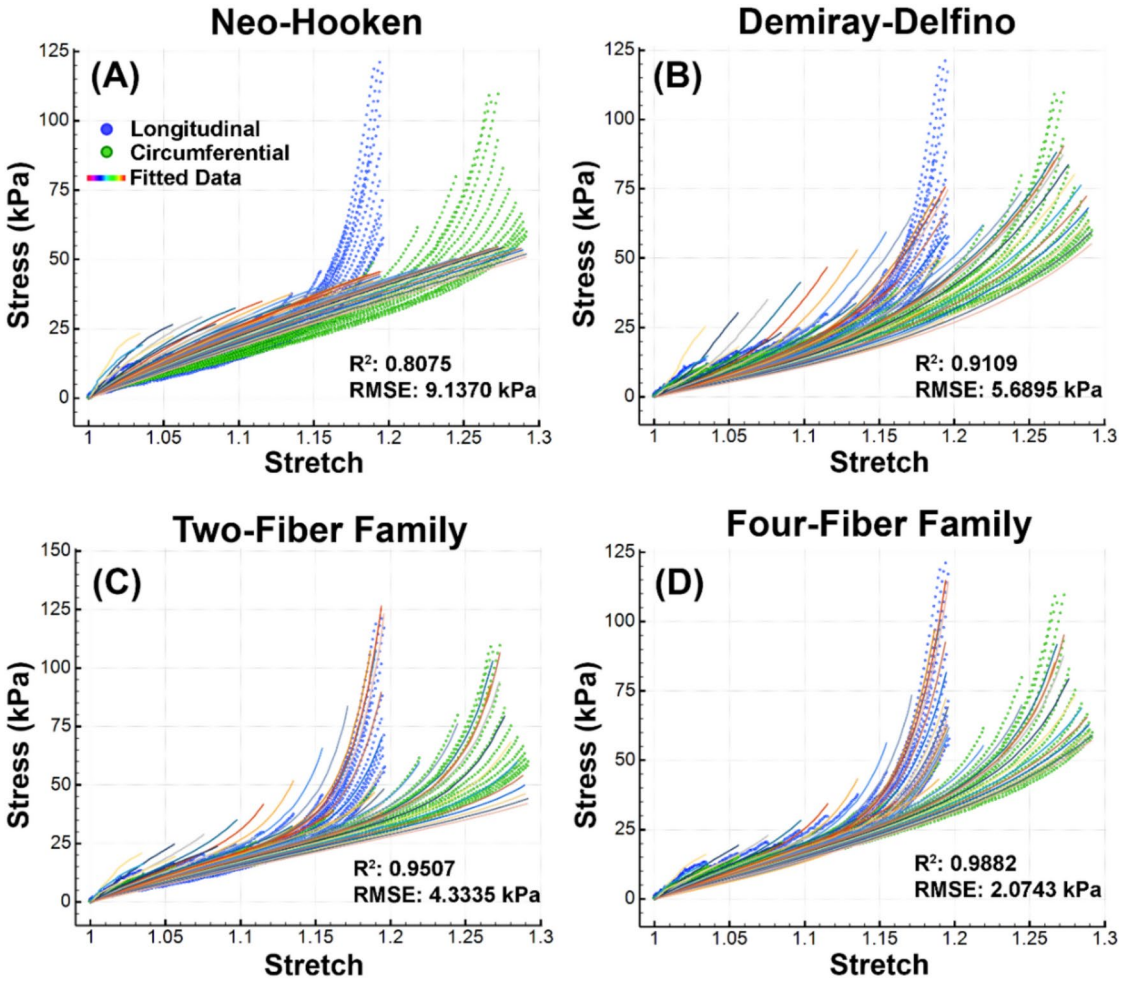

Fig. 5. The experimental Cauchy stress–stretch curves of S7 (67 years old male) at descending thoracic aorta (TA) obtained from the 19 biaxial loading protocols and the fitted (**A**) neo-Hookean, (**B**) Demiray-Delfino, (**C**) two-fiber family, and (**D**) four-fiber family model in the longitudinal and circumferential directions.

family ranged from 2.165 to 23.694 kPa (6.574 ± 4.667 kPa), Demiray-Delfino ranged from 1.817 to 26.940 kPa (7.681 ± 5.900 kPa), and neo-Hookean model ranged from 4.254 to 62.029 kPa (15.915 ± 12.877 kPa) for all samples. The constitutive parameters for the four-fiber family model are provided in Table 1. The constitutive parameters for the two-fiber family, Demiray-Delfino, and neo-Hookean models are presented in the Supplement, Tables S2, S3, S4.

Histological analysis

Histological analysis of aortic samples from four locations along the aorta, stained with Movat's Pentachrome, revealed changes in elastin and GAGs density and structural architecture from the TA to the dAA. Figure 6 illustrates these differences, showing stained ring samples from S5 (60 F) across all four locations. In the proximal locations (TA and SC), elastin lamellae (black) appeared more continuous, thicker, and undulated, resembling closely arranged sheets encircling the aorta. Moving distally (IFR and dAA), the elastin lamellae became progressively thinner and less continuous, with visible discontinuities between the lamellar sheets as they circumscribe the aorta. The distance between lamellae (interlamellar space) increased, and the sheets displayed a wavier structure. These visual observations were supported by quantitative measurements. Elastin density results are presented in Fig. 7A. Elastin density in tunica media experienced a significant decline along

Subject	Anatomical Location	c_{gr}(kPa)	$c_1^1 = c_1^2$(kPa)	$c_2^1 = c_2^2$	c_1^3(kPa)	c_2^3	c_1^4(kPa)	c_2^4	γ°	RMSE (kPa)	R^2
S1	TA	18.458	12.151	15.754	23.286	4.888	11.912	12.922	40.539	1.995	0.989
	SC	26.476	6.503	67.277	33.507	13.519	9.157	34.005	38.182	1.463	0.986
	IFR	76.965	76.506	170.879	20.967	73.918	144.912	235.870	52.685	5.191	0.957
	dAA	76.829	139.641	230.546	159.950	310.017	22.381	116.588	53.789	3.309	0.963
S2	TA	23.162	21.143	19.980	44.885	7.791	16.549	33.742	68.221	1.243	0.995
	SC	21.453	96.593	86.332	6.544	3.117	216.092	62.202	23.904	7.958	0.942
	IFR	31.301	71.406	180.768	113.975	126.322	6.798	78.031	46.211	2.593	0.909
	dAA	37.058	37.349	170.100	108.075	140.431	82.137	193.318	44.307	1.727	0.941
S3	TA	44.920	7.406	10.120	11.145	1.974	21.336	10.633	39.384	1.840	0.996
	SC	55.059	6.634	15.908	15.046	3.013	38.269	7.471	39.068	1.346	0.998
	IFR	39.225	24.731	19.421	12.856	9.553	56.986	14.645	35.916	3.073	0.993
	dAA	38.698	32.870	53.718	13.762	22.155	67.050	54.139	39.473	1.687	0.994
S4	TA	10.105	13.612	1.762	17.187	0.443	10.736	1.433	52.630	1.637	0.994
	SC	16.656	2.007	26.853	10.281	10.036	5.374	10.994	44.906	0.681	0.997
	IFR	8.486	7.829	13.773	11.313	6.925	16.291	6.810	40.790	0.551	0.998
	dAA	7.815	12.725	7.730	17.086	2.709	8.454	6.222	42.344	0.689	0.995
S5	TA	7.422	3.308	2.777	10.700	0.131	8.079	2.919	37.059	1.511	0.992
	SC	13.417	3.653	8.055	8.942	2.009	2.683	6.755	42.017	4.289	0.965
	IFR	7.672	2.575	14.584	2.777	7.055	11.333	10.464	43.784	2.079	0.986
	dAA	8.742	2.632	35.264	16.922	27.299	6.308	5.469	49.480	1.314	0.986
S6	TA	13.121	14.700	22.224	14.942	2.648	10.185	46.056	26.532	2.580	0.980
	SC	135.494	126.748	120.732	44.690	0.786	226.649	175.989	55.069	18.098	0.817
S7	TA	26.156	1.321	15.303	13.101	1.284	5.748	12.526	39.466	2.074	0.988
	SC	29.023	3.017	15.282	17.253	2.733	7.209	7.938	41.944	1.330	0.996
	IFR	31.361	82.947	83.656	58.518	40.519	23.436	85.557	42.618	3.638	0.981
	dAA	0.040	42.804	77.307	42.416	137.067	8.041	68.435	55.338	5.650	0.886
S8	TA	25.952	10.049	1.305	24.302	0.260	8.714	0.671	39.561	1.777	0.998
	SC	28.572	2.922	5.583	23.955	0.148	4.833	2.935	32.229	1.098	0.998
	IFR	25.635	1.275	12.743	12.084	1.230	6.194	12.231	42.614	1.647	0.993
	dAA	25.879	2.703	17.956	4.432	5.379	7.893	12.185	37.873	1.042	0.997
S9	TA	45.929	21.161	14.230	29.702	9.159	19.629	12.054	47.307	16.147	0.933
	SC	30.475	4.215	19.390	15.975	4.959	15.645	9.743	41.146	1.805	0.994
	IFR	12.829	11.569	49.188	42.598	53.078	3.806	16.608	46.278	2.915	0.975
	dAA	1.800	27.428	28.317	32.010	37.309	16.852	8.532	51.178	3.602	0.940
S10	TA	50.655	5.957	11.506	35.105	1.069	10.701	10.333	34.378	6.460	0.988
	SC	27.997	5.626	9.669	16.094	0.634	13.405	10.409	32.844	2.943	0.992
	IFR	53.391	10.232	27.898	19.834	14.422	20.311	11.560	43.927	5.888	0.982
	dAA	9.201	10.309	41.470	43.368	17.723	20.734	18.625	47.860	1.673	0.990

Table 1. Constitutive parameters for the four-fiber family model describing multi-ratio biaxial responses of TA, SC, IFR, and dAA in 10 subjects. 19 different unique loading protocols were used to determine constitutive parameters.

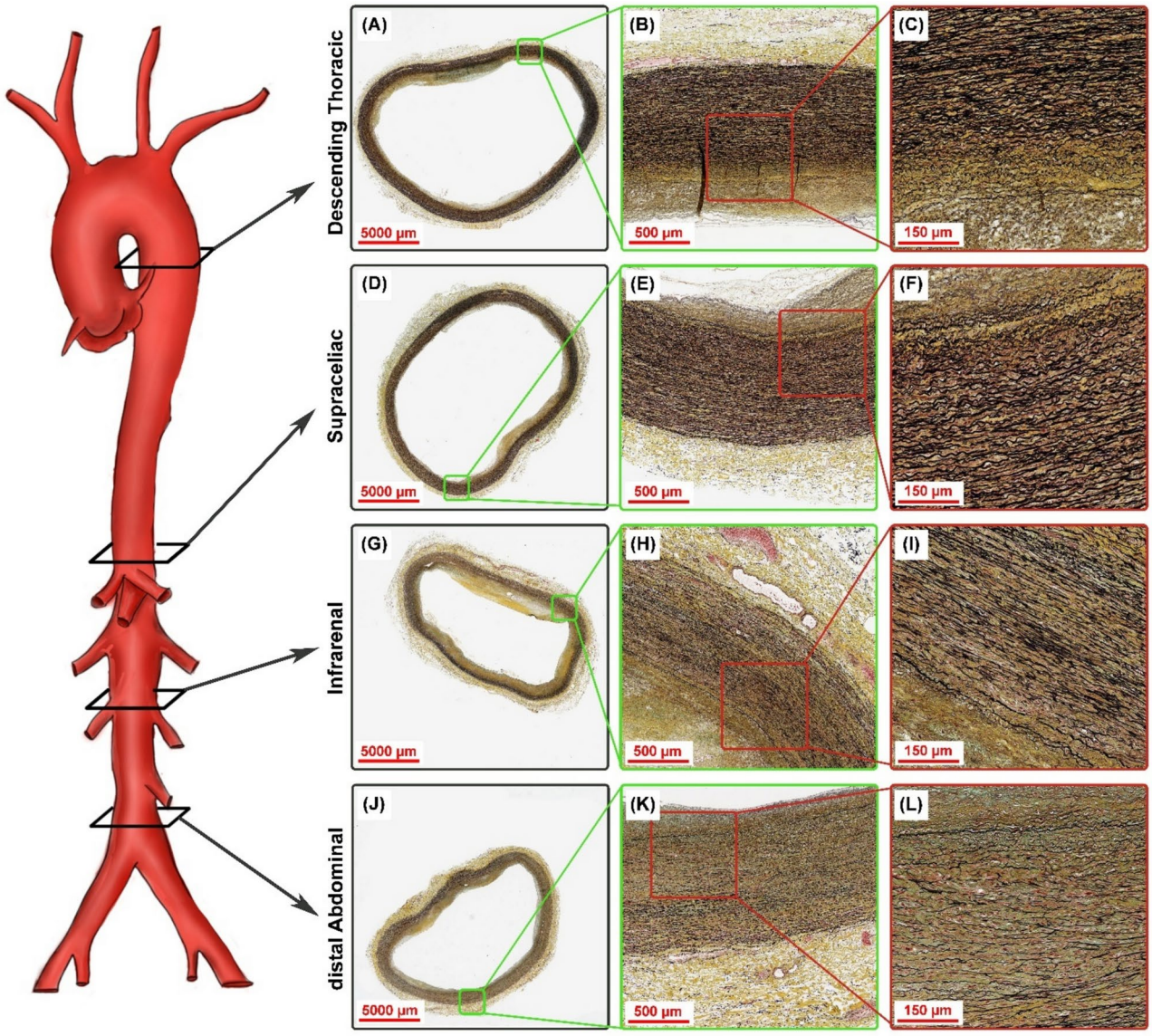

Fig. 6. The internal structure of a representative subject aorta (S5: 60 years old female) at four different locations (**A**, **D**, **G** and **J**) stained with MOVAT's Pentachrome (elastin: black—glycosaminoglycans (GAG): greenish-gray) in circumferential planes. The left column (**A**, **D**, **G** and **J**) shows the distribution of structural components within the the ring sample, while the middle (**B**, **E**, **H** and **K**) and right columns (**C**, **F**, **I** and **L**) present magnified images to better illustrate the elastin and GAGs distribution and architecture. Note the larger interlamellar spaces and more degraded elastin in the more distal specimen.

the aortic length: 23.54% in TA, 21.52% in SC, 12.44% in IFR, and 8.96% in dAA. A GG-corrected RM ANOVA revealed a highly significant effect of location on elastin density ($p < 0.001$), with notable differences between TA and IFR ($p < 0.001$), TA and dAA ($p < 0.001$), SC and IFR ($p < 0.001$), and SC and dAA ($p < 0.001$). The Movat staining also revealed GAGs distribution in the aortic wall. GAGs (greenish-gray) were primarily located in the thickened intima and within the media, particularly near the internal elastic lamina. They were concentrated in the interlamellar spaces, especially where elastic sheets were degraded. GAGs density, shown in Fig. 7B, was consistent across all locations at approximately 5–6%, with no significant differences along the aortic length ($p = 0.364$).

Since the intrinsic stiffness of the aortic wall is influenced by its structural composition, we examined the statistical correlation between linear stiffness (both low- and high-range stiffness) and the density of elastin and GAGs, as shown in Fig. 7C and D, respectively. Stiffness increased significantly with decreasing elastin density in the media, with an $R^2 = 0.246$ and $p = 0.010$ for high-range stiffness and $R^2 = 0.263$ and $p = 0.004$ for low-range stiffness. In contrast, changes in GAGs density did not have a significant effect on either high- or low-range stiffness ($R^2 = 0.022$, $p = 0.465$ for high-range stiffness and $R^2 = 0.0$, $p = 0.958$ for low-range stiffness).

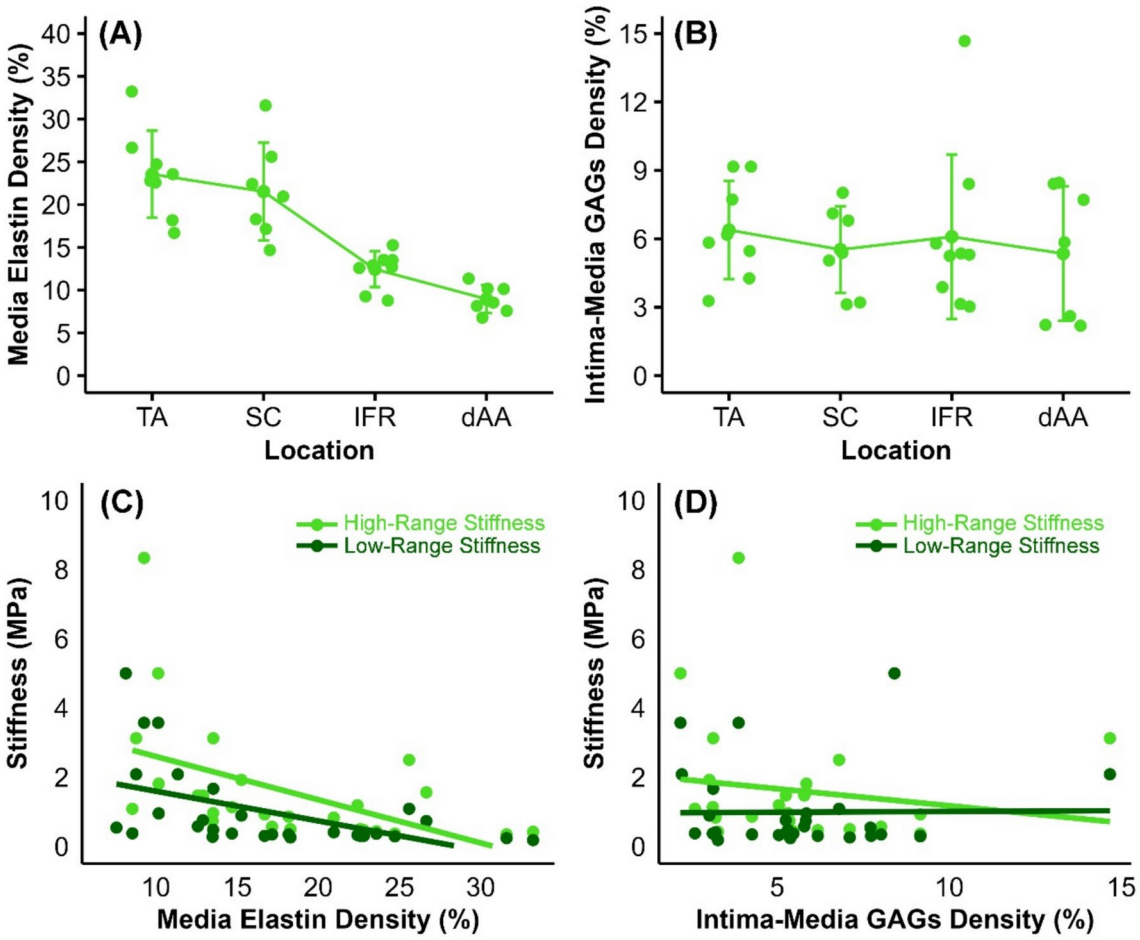

Fig. 7. (**A**) Media elastin density and (**B**) intima-media GAGs density across aortic locations (TA: descending Thoracic Aorta, SC: Supraceliac Aorta, IFR: Infrarenal Aorta, dAA: distal Abdominal Aorta). Elastin density shows a significant decreasing trend from thoracic to abdominal regions, reflecting structural degradation along the aortic length. In contrast, GAGs density remains relatively consistent across locations. Each plot shows individual data points (colored dots) for each subject along with the mean ± standard deviation (solid lines with error bars). (**C**) Correlation between media elastin density and intrinsic linear stiffness (low-range: 25–50 kPa, high-range: 50–75 kPa). A significant negative correlation is observed, indicating that as elastin density decreases, stiffness increases, suggesting a shift from elastin-dominated to collagen-dominated mechanical behavior in distal aortic segments. (**D**) Correlation between intima-media GAGs density and intrinsic linear stiffness. No significant relationship is observed between GAGs density and stiffness metrics.

Discussion

Cardiovascular diseases and aortic pathologies are driven not only by biological changes in the aortic wall but also by alterations in its morphometrical and mechanical properties. Mechanical factors such as wall stress and aortic stiffening play a critical role in the onset and progression of conditions like aortic aneurysms, dissections, and hypertension[3]. Aorta's geometry and mechanical properties vary along its length, influenced by increasing distance from the heart and regional functional demands. This regional heterogeneity leads to variations in the development, progression, and mechanisms of aortic diseases between segments such as the thoracic and abdominal aorta[6]. Understanding these location-dependent characteristics is crucial for evaluating their potential impact on disease development. Furthermore, such knowledge is essential for advancing targeted therapeutic approaches tailored to each aortic segment. In this study, we comprehensively investigated the mechanical, structural, and morphological properties of the human aorta at four clinically significant locations: the TA, SC, IFR, and dAA. These locations were selected due to their susceptibility to aneurysms, dissections, and plaque formation. Using fresh human aortas from middle-aged and elderly donors—populations most vulnerable to aortic pathologies—we assessed these properties across locations within the same subjects. To complement these findings, we also provided parameters for four commonly used constitutive models, offering a foundation for computational simulations and clinical applications.

An understanding of aortic geometry is crucial, as it directly influences blood flow dynamics, risk assessment for aortic pathologies, and the design of endovascular devices such as stent-grafts. Our study demonstrated a clear decreasing trend in both inner and outer diameters along the aortic length, with the most pronounced

reductions observed between the thoracic (outer: 12.72 mm, inner: 9.30 mm) and infrarenal regions (outer: 9.71 mm, inner: 6.53 mm). Beyond the infrarenal aorta, diameters stabilized in the distal segments. This trend aligns with previous findings from both ex-vivo and in-vivo studies. For instance, Kamenskiy et al. observed that the outer diameter of human aortas decreased from 11.18 mm in the thoracic region to 8.14 mm in the abdominal aorta in middle-aged individuals[11]. Similarly, porcine ex-vivo studies have reported inner diameters of ~ 7–8 mm in the upper thoracic aorta, decreasing to ~ 4–5 mm in the abdominal aorta[7,12,21,27]. These smaller dimensions in porcine aortas are expected, as the samples are typically from younger animals, whereas human aortas in our study were from middle-aged and elderly individuals, where aging is known to increase aortic diameters[5,45]. In-vivo human studies have shown similar patterns, though with a wider range of values due to methodological differences such as imaging modalities (e.g., CT, MRI, ecocardiography) and timing within the cardiac cycle (systole or diastole). These studies report outer radii ranging from ~ 12–13.5 mm in the upper thoracic aorta to ~ 9.5–12 mm near the diaphragm, and ~ 9–10 mm in the infrarenal and ~ 8.5–10 mm distal abdominal aorta[14,15,19,45–48]. Our measurements fall within these ranges for all locations.

Similarly, our results demonstrated a slight decreasing trend in load-free aortic wall thickness as the aorta transitions toward the periphery, with values declining from 3.10 mm in the TA to 2.91 mm at the SC, 2.80 mm at the IFR, and 2.77 mm at the dAA. This trend is most pronounced when comparing the proximal thoracic region to the distal abdominal segments. The observed reduction in wall thickness aligns with the more pronounced decrease in outer radii relative to inner radii along the length of the aorta. This location-dependent decrease in wall thickness aligns with previous findings. Peña et al.[12] reported thicknesses of 2.46 mm and 1.57 mm in the upper and lower thoracic aorta of porcine models, respectively, while Sokolis et al.[21] observed a decrease from 1.7 mm in the upper thoracic region to ~ 1 mm in the lower thoracic and abdominal segments in porcine aortas. Similarly, Kamenskiy et al.[11] found 2.63 mm in the TA and 2.04 mm in the dAA in humans. An in-vivo study of 753 subjects further confirmed thicker walls in the proximal thoracic aorta compared to distal regions[46].

The observed changes in radii and wall thickness collectively reflect the tapering nature of the aorta, a critical adaptation for maintaining efficient hemodynamic performance as the vessel transitions along its length. Larger diameters and thicker walls in the proximal thoracic regions accommodate higher pulsatile loads and facilitate energy storage near the heart. In contrast, the reduced dimensions in the distal abdominal regions align with the shift to muscular properties, optimizing blood flow and pressure dynamics for efficient downstream perfusion[35].

Measurement of aortic wall thickness differences in load-free and stress-free configurations ex-vivo provides valuable insights into the mechanical residual stresses within the aortic wall. Residual stress is a critical factor in understanding the mechanical behavior of arterial walls, as it reflects ECM remodeling, growth, and plays a vital role in redistributing wall stress circumferentially[40]. Our results demonstrated that the wall thickness of stress-free cut-ring samples was consistently higher than that of load-free ring samples. Wall thickness in stress-free configuration varied across locations, showing a trend different from the thickness of load-free aortas. While a slight decrease was observed from the TA to the SC segment, the thickness in stress-free configuration exhibited a marked increase in the IFR and dAA. This increase in H in distal arteries, coupled with the observed decrease in h along the aortic length, results in a significant difference between the two configurations for both the IFR (1.3 mm) and dAA (1.16 mm). These results indicate higher circumferential residual deformations in the distal segments of the aorta. These findings align with previous studies reporting the greatest geometric changes between load-free and stress-free configurations in the abdominal aorta[27].

The changes in opening angle with location further corroborate the thickness results. The opening angle, is a direct marker of circumferential residual stress. We observed that the opening angle increased from the TA to the IFR before decreasing in the dAA. The highest opening angle was noted in the upper abdominal segment (e.g. IFR), consistent with the largest difference between h and H in this location. Conversely, the TA exhibited the lowest differences in thicknesses as well as the lowest opening angle. These findings align with prior porcine and human studies, where ascending aortas and abdominal segments typically exhibited higher opening angles than descending thoracic segments[11,12,27,49]. Interestingly, the range of human opening angle values is approximately three times greater than those reported in porcine and murine models. This discrepancy likely stems from species-specific differences in geometry, curvature, and diameter. The higher opening angle in the abdominal aorta suggests that circumferential residual stresses are more effectively rebalanced in this region, potentially reflecting a greater imbalance between the intimal and adventitial layers in these segments[49,50]. This imbalance was further supported by our observation that intimal lengths exceeded adventitial lengths in cut-ring samples. This finding is consistent with prior studies, such as those by Peña et al.[12], which quantified layer-specific residual deformations in porcine aortas. Their results showed that the intimal opening angle was significantly greater than that of the adventitia, explaining the outward curving tendency of aortic segments in both our study and previous reports. These observations underscore the critical role of residual stresses in maintaining arterial wall integrity and adapting to regional hemodynamic demands.

In terms of ECM structural changes along the aorta length, we observed a significant decreasing trend in elastin density, with proximal segments (e.g., TA and SC) showing nearly double the elastin density compared to distal segments (e.g., IFR and dAA) (proximal: ~ 20–25% vs. distal: ~ 10–15%). Beyond this quantitative reduction, qualitative differences in elastin architecture were also apparent. In the TA and SC, elastin was organized into thick, continuous sheets, closely packed and circumferentially aligned. In contrast, in the IFR and dAA, the elastin sheets were thinner, fragmented, and less continuous. Elastin in the proximal regions (e.g., TA and SC) was more uniformly distributed throughout the media, contributing to the wall's buffering capacity. Conversely, in distal locations (e.g., IFR and dAA), medial elastin was predominantly concentrated near the tunica intima and tunica adventitia. Notably, changes in a single ECM component rarely occur in isolation; they are typically accompanied by alterations in other components[51]. The interplay between elastin and collagen is particularly crucial, as these components are tightly coupled in determining wall mechanics[52]. The distal

degradation and reduction of elastin are often compensated by collagen recruitment, a process that shifts the mechanical dominance from elastin in proximal segments to collagen in distal segments[8,21,27].

In the proximal aorta, such as the TA and SC, elastin dominates the mechanical response of the arterial wall. Elastin is a highly resilient material, enabling the vessel to store and release energy efficiently, facilitating recoil during diastole, and supporting the Windkessel mechanism. The abundance of elastin in these regions also explains the lower opening angles observed proximally. Even after radial cuts, the pre-stretched elastin sheets maintain the arterial wall's circular geometry[36,51]. Conversely, the distal aorta (e.g., IFR and dAA) exhibits a lower elastin-to-collagen ratio. Collagen, being stiffer and less elastic, resists the recoil of pre-stretched elastin, resulting in higher opening angles and reduced compliance in these segments[24,36,53]. We also found that, in regions with lower elastin density (more distal locations), the difference between low- and high-range stiffness was more pronounced. This is likely due to the earlier engagement of collagen fibers in load-bearing. In contrast, elastin-rich regions exhibited a more gradual transition, highlighting elastin's role in maintaining a consistent mechanical response and reducing non-linear stiffening[25,54]. The higher collagen content in distal regions likely reflects the aorta's natural remodeling to optimize geometry and mechanics for local hemodynamic demands. While elastin-rich proximal segments support compliance and pulsatility to reduce cardiac load, the collagen-enriched distal segments create impedance mismatches that reflect pressure waves back toward the heart, minimizing transmission to peripheral vasculature. This regional adaptation helps maintain overall hemodynamic efficiency[27,35].

GAGs, an essential component of the arterial wall, were also analyzed in this study. These molecules are largely absent in young aortas but increase with age, filling the gaps created by the breakdown of the elastin network[55,56]. In our samples, GAGs were distributed non-uniformly, with the highest concentration near the thickened intima, consistent with previous studies[55]. Despite this variability, GAGs density remained relatively constant (~ 5–6%) along the length of the aorta. Based on this observation and the previously reported increase in collagen density in distal segments, collagen-to-GAG ratio may increase distally. This ratio, introduced by Ghadie et al.[57], was shown to correlate strongly with the opening angle in the proximal thoracic aorta and the arch of porcine aortas. Their findings indicated that moving from the arch to the descending thoracic aorta, an increase in the collagen-to-GAG ratio was accompanied by a decrease in the opening angle. Interestingly, our study contrasts with this trend, as we observed that in the abdominal aorta, an increase in the collagen-to-GAG ratio corresponded to an increase in the opening angle. This discrepancy may arise from the fact that Ghadie et al. 's study focused exclusively on the thoracic aorta[57], whereas our research includes both thoracic and abdominal regions. This broader focus may capture regional differences in aortic remodeling processes that vary along the aortic length. Regardless of these differences, the collagen-to-GAG ratio is significant as it reflects aortic remodeling in response to elastin degradation and indicates the relative contributions of GAGs and collagen to this process. GAGs are believed to influence residual stresses in the arterial wall through their swelling pressure, counterbalancing the tension between elastin and collagen fibers[57]. This interaction likely affects the pre-stretch level of these fibers, which, in turn, impacts the residual stresses and opening angles upon radial cutting. These complex structural and mechanical interactions warrant further investigation to fully understand the role of GAGs and collagen in aortic remodeling along its entire length.

Beyond the geometrical and structural changes along the aorta, its mechanical properties also varied significantly along its length. All tested arteries exhibited anisotropic and nonlinear behavior, with stiffness increasing exponentially at higher stretches. Our biaxial testing revealed that the distal aortic segments were significantly stiffer than the proximal ones at physiological and higher stress levels. In most cases, whether in the longitudinal or circumferential direction, one of the distal segments (IFR or dAA) consistently emerged as the stiffest along the aortic length. Notably, the differences between locations were most pronounced at higher stress levels. At low stress (25 kPa), proximal and distal segments demonstrated comparable stretch responses. However, at higher stresses (50 and 75 kPa), proximal segments exhibited greater compliance and stretchability in both directions. This was further supported by the linear stiffness metrics, where high-range stiffness exhibited more pronounced location-based differences compared to low-range stiffness.

These findings align with previous ex-vivo studies employing planar biaxial, uniaxial, and inflation-extension testing on both porcine and human aortas, which similarly observed that distal locations are generally stiffer than proximal ones, with differences becoming more apparent at higher stretches[8,11,21,27]. This location-specific behavior can be explained by variations in the distribution and architecture of collagen and elastin along the aorta. Moving distally, the increasing abundance of stiff collagen fibers and the decreasing density of elastic fibers and lamellae result in greater intrinsic stiffness. At lower stretches, applied pressures predominantly straighten fibers without significant stretching, minimizing differences in mechanical behavior across locations. However, at higher pressures, such as those experienced during systole, both elastic and collagen fibers begin to stretch and straighten, making their mechanical properties the dominant factor. In distal locations, where the collagen-to-elastin ratio is higher, the greater contribution of stiff collagen fibers results in markedly stiffer behavior.

Regarding anisotropy, our study found no significant differences between the longitudinal and circumferential directions across most locations and stress levels, except for thoracic regions (TA and SC) at the highest stress levels. While not statistically significant, our samples exhibited slightly greater compliance in the circumferential direction. Interestingly, these results are consistent with findings from human studies by Kamenskiy et al.[11] and Haskett et al.[8], but they contrast with porcine studies, which have reported greater anisotropy in distal segments, with the circumferential direction being stiffer than the longitudinal[21,27]. This discrepancy is likely due to the lack of age-related effects in porcine aortas. It is well-established that in younger humans, thoracic aortas are relatively isotropic, as both directions are highly compliant. However, with aging, the longitudinal direction stiffens more rapidly, resulting in increased anisotropy in individuals over 50 years of age, where the longitudinal direction becomes stiffer[5]. In contrast, abdominal aortic segments contain more collagen fibers, which are predominantly aligned circumferentially[24,27]. This alignment is expected to result in faster stiffening in

the circumferential direction compared to thoracic segments. Such structural differences and remodeling likely account for the lack of pronounced anisotropy observed in the distal segments of human aortas in this study.

The higher stiffness observed in distal segments is consistent with in-vivo studies, which have long reported an increase in PWV from the heart to the peripheries[15,17,19]. PWV is a critical index of arterial stiffness in-vivo and is influenced not only by mechanical properties but also by geometrical features. According to the Moens-Kortweg equation ($PWV = \sqrt{\frac{E \cdot h}{2r\rho}}$), PWV is a function of wall elastic modulus (E), blood density (ρ) and the wall thickness-to-inner radius ratio ($\frac{h}{r}$). Based on our findings, the $\frac{h}{r}$ ratio showed an increasing trend from proximal to distal segments, with values of 0.34, 0.38, 0.43, and 0.42 for TA, SC, IFR, and dAA, respectively. Additionally, biaxial testing revealed that the intrinsic elastic modulus of the aortic wall also increased distally. The combination of these mechanical and geometric changes contributes to the tapering of the aorta along its length, leading to higher impedance and elevated PWV in distal segments.

We utilized our experimental data to determine constitutive model parameters for all arteries across four locations, employing four widely used strain energy functions: neo-Hookean, Demiray-Delfino, two-fiber family, and four-fiber family models. The four-fiber family model extends the well-established two-fiber family model originally introduced by Holzapfel and Ogden (HGO)[58]. While these models are phenomenological, they are informed by the general organization of arterial wall constituents[11,59]. Among the models tested, the four-fiber family model exhibited the best fit to our experimental data, as evidenced by its lower RMSE and higher R^2 values. Both the two-fiber family and Demiray-Delfino models also provided reasonably accurate fits, despite having fewer parameters. These constitutive parameters can be instrumental in computational studies, offering insights into vascular physiology and pathophysiology.

While our study provides valuable insights into the mechanical, structural, and geometrical characteristics of the human aorta along its length, several limitations should be acknowledged to contextualize the findings and guide future research. First, a complete understanding of aortic variations along its length would benefit from the inclusion of the ascending aorta and arch segments, as these proximal regions are closest to the heart and play a critical role in preserving the aorta's Windkessel function, hemodynamic efficiency, and physiological regulation. Unfortunately, most of the harvested aortas obtained from the organ procurement organization lacked these segments, precluding their analysis in this study. Second, previous studies, including our prior research, have demonstrated circumferential heterogeneity in aortic mechanical properties, suggesting that regional differences around the circumference may also contribute to axial variations along the length of the aorta[26,60]. However, in this study, we specifically focused on axial differences by testing the lateral quadrant of each segment to ensure consistency in comparing mechanical properties across different anatomical locations. Third, we did not investigate the impact of risk factors such as age, sex, diabetes, and hypertension, as our sample size was insufficient to draw meaningful conclusions regarding these variables. However, the influence of these factors is well-documented in existing literature[61]. Fourth, due to disease spread in distal segment of S6, we were unable to analyze all regions for this subject. Fifth, the age of the subjects in this study, primarily middle-aged and older individuals, limits the generalizability of the findings to younger populations. Given that the dAA is often one of the first regions to develop vascular disease[62], some of the observed stiffness in this segment could be attributed to age-related disease processes rather than intrinsic mechanical properties. Studies on younger aortas are needed to understand how regional stiffness changes with age and disease. Sixth, our study relied on phenomenological constitutive models to characterize aortic mechanical properties and these models do not explicitly account for microstructural components such as elastin, collagen, and GAGs. Future studies could benefit from incorporating structure-based constitutive models to provide a more mechanistic understanding of how histological composition influences arterial wall mechanics[63]. Lastly, we assumed the aortic wall to be homogeneous without distinguishing between the intima, media, and adventitia layers. While this assumption is common in many studies, it overlooks the well-established differences in the structural and mechanical properties of these layers, which could provide additional insights into aortic behavior and disease progression[12,50,64].

Conclusions

This study provides a comprehensive evaluation of the regional mechanical, morphological, and structural properties of the human aorta, highlighting significant differences along its length. Distal segments exhibited higher stiffness and greater residual stresses, accompanied by a pronounced decline in elastin density and lamellar continuity. Morphometric analysis further revealed location-specific changes in wall thickness and opening angles, underscoring the heterogeneous adaptations of the aorta to varying hemodynamic demands. These findings enhance our understanding of the biomechanical and structural complexity of the human aorta, offering valuable parameters for computational modeling and guiding the development of site-specific vascular therapies.

Data availability

The datasets used and/or analyzed during the current study available from the corresponding author on reasonable request.

Received: 11 December 2024; Accepted: 18 March 2025
Published online: 01 April 2025

References

1. Westerhof, N., Lankhaar, J.-W. & Westerhof, B. E. The arterial Windkessel. *Med. Biol. Eng. Comput.* **47**, 131–141 (2009).

2. Belz, G. G. Elastic properties and Windkessel function of the human aorta. *Cardiovasc. Drug Ther.* **9**, 73–83 (1995).
3. Cecelja, M. & Chowienczyk, P. Role of arterial stiffness in cardiovascular disease. *JRSM Cardiovasc. Dis.* **1**, 1–10 (2012).
4. Said, M. A., Eppinga, R. N., Lipsic, E., Verweij, N. & Van Der Harst, P. Relationship of arterial stiffness index and pulse pressure with cardiovascular disease and mortality. *JAHA* **7**, e007621 (2018).
5. Jadidi, M. et al. Mechanical and structural changes in human thoracic aortas with age. *Acta Biomater.* **103**, 172–188 (2020).
6. Chowienczyk, P. J. Aortic stiffness and disease: Location is key. *Circulation* **131**, 1745–1747 (2015).
7. Guo, X. & Kassab, G. S. Variation of mechanical properties along the length of the aorta in C57bl/6 mice. *Am. J. Physiol.-Heart Circul. Physiol.* **285**, H2614–H2622 (2003).
8. Haskett, D., Johnson, G., Zhou, A., Utzinger, U. & Vande Geest, J. Microstructural and biomechanical alterations of the human aorta as a function of age and location. *Biomech. Model Mechanobiol.* **9**, 725–736 (2010).
9. LeMaire, S. A. & Russell, L. Epidemiology of thoracic aortic dissection. *Nat. Rev. Cardiol.* **8**, 103–113 (2011).
10. Guo, D., Papke, C. L., He, R. & Milewicz, D. M. Pathogenesis of thoracic and abdominal aortic aneurysms. *Ann. N. Y. Acad. Sci.* **1085**, 339–352 (2006).
11. Kamenskiy, A. V. et al. Biaxial mechanical properties of the human thoracic and abdominal aorta, common carotid, subclavian, renal and common iliac arteries. *Biomech. Model Mechanobiol.* **13**, 1341–1359 (2014).
12. Peña, J. A., Martínez, M. A. & Peña, E. Layer-specific residual deformations and uniaxial and biaxial mechanical properties of thoracic porcine aorta. *J. Mech. Behav. Biomed. Mater.* **50**, 55–69 (2015).
13. García, A. et al. Experimental study and constitutive modelling of the passive mechanical properties of the porcine carotid artery and its relation to histological analysis: Implications in animal cardiovascular device trials. *Med. Eng. Phys.* **33**, 665–676 (2011).
14. Rogers, W. J. et al. Age-associated changes in regional aortic pulse wave velocity. *J. Am. Coll. Cardiol.* **38**, 1123–1129 (2001).
15. Kim, E. K. et al. Assessment of regional aortic stiffness with cardiac magnetic resonance imaging in a healthy Asian population. *Int. J. Cardiovasc. Imaging* **29**, 57–64 (2013).
16. Soulat, G. et al. Changes in segmental pulse wave velocity of the thoracic aorta with age and left ventricular remodelling. An MRI 4D flow study. *J. Hypertension* **38**, 118–126 (2020).
17. Devos, D. G. H. et al. MR pulse wave velocity increases with age faster in the thoracic aorta than in the abdominal aorta. *J. Magn. Reson. Imaging : JMRI* **41**, 765–772 (2015).
18. Wong, D. T. L. et al. Regional aortic distensibility and its relationship with age and aortic stenosis: A computed tomography study. *Int. J. Cardiovasc. Imaging* **31**, 1053–1062 (2015).
19. Hickson, S. S. et al. The relationship of age with regional aortic stiffness and diameter. *JACC Cardiovasc. Imag.* **3**, 1247–1255 (2010).
20. Lillie, M. A. & Gosline, J. M. Mechanical properties of elastin along the thoracic aorta in the pig. *J. Biomech.* **40**, 2214–2221 (2007).
21. Sokolis, D. P. Passive mechanical properties and structure of the aorta: segmental analysis. *Acta Physiol.* **190**, 277–289 (2007).
22. Kim, J., Hong, J. & Baek, S. Longitudinal differences in the mechanical properties of the thoracic aorta depend on circumferential regions. *J. Biomed. Mater. Res.* **101A**, 1525–1529 (2013).
23. Azadani, A. N. et al. Comparison of mechanical properties of human ascending aorta and aortic sinuses. *Ann. Thorac. Surg.* **93**, 87–94 (2012).
24. Zeinali-Davarani, S., Wang, Y., Chow, M.-J., Turcotte, R. & Zhang, Y. Contribution of collagen fiber undulation to regional biomechanical properties along porcine thoracic aorta. *J. Biomech. Eng.* **137**, 051001 (2015).
25. Peña, J. A., Corral, V., Martínez, M. A. & Peña, E. Over length quantification of the multiaxial mechanical properties of the ascending, descending and abdominal aorta using digital image correlation. *J. Mech. Behav. Biomed. Mater.* **77**, 434–445 (2018).
26. Sokolis, D. P., Bompas, A., Papadodima, S. A. & Kourkoulis, S. K. Variation of axial residual strains along the course and circumference of human aorta considering age and gender. *J. Biomech. Eng.* **142**, 021003 (2020).
27. Dwivedi, K. K. et al. Location specific multi-scale characterization and constitutive modeling of pig aorta. *J. Mech. Behav. Biomed. Mater.* **142**, 105809 (2023).
28. Harloff, A. et al. Determination of aortic stiffness using 4D flow cardiovascular magnetic resonance - a population-based study. *J. Cardiovasc. Magn. Reson.* **20**, 43 (2018).
29. Markl, M. et al. Analysis of pulse wave velocity in the thoracic aorta by flow-sensitive four-dimensional MRI: Reproducibility and correlation with characteristics in patients with aortic atherosclerosis. *Magn. Reson. Imaging* **35**, 1162–1168 (2012).
30. Ohyama, Y. et al. Aortic arch pulse wave velocity assessed by magnetic resonance imaging as a predictor of incident cardiovascular events: The mesa (multi-ethnic study of atherosclerosis). *Hypertension* **70**, 524–530 (2017).
31. Bersi, M. R. et al. Novel methodology for characterizing regional variations in the material properties of murine aortas. *J. Biomech. Eng.* **138**, 071005 (2016).
32. Bersi, M. R., Bellini, C., Humphrey, J. D. & Avril, S. Local variations in material and structural properties characterize murine thoracic aortic aneurysm mechanics. *Biomech. Model Mechanobiol.* **18**, 203–218 (2019).
33. Bersi, M. R. et al. Multimodality imaging-based characterization of regional material properties in a murine model of aortic dissection. *Sci. Rep.* **10**, 9244 (2020).
34. Farzaneh, S., Trabelsi, O. & Avril, S. Inverse identification of local stiffness across ascending thoracic aortic aneurysms. *Biomech. Model Mechanobiol.* **18**, 137–153 (2019).
35. Rachev, A., Greenwald, S. & Shazly, T. Are geometrical and structural variations along the length of the aorta governed by a principle of "optimal mechanical operation"?. *J. Biomech. Eng.* **135**, 081006 (2013).
36. Lillie, M. A., Armstrong, T. E., Gérard, S. G., Shadwick, R. E. & Gosline, J. M. Contribution of elastin and collagen to the inflation response of the pig thoracic aorta: Assessing elastin's role in mechanical homeostasis. *J. Biomech.* **45**, 2133–2141 (2012).
37. Dinardo, C. L. et al. Variation of mechanical properties and quantitative proteomics of VSMC along the arterial tree. *Am. J. Physiol.-Heart Circ. Physiol.* **306**, H505–H516 (2014).
38. Martin, C., Pham, T. & Sun, W. Significant differences in the material properties between aged human and porcine aortic tissues. *Eur. J. Cardiothorac. Surg.* **40**, 28–34 (2011).
39. Duca, L. et al. Matrix ageing and vascular impacts: Focus on elastin fragmentation. *Cardiovasc. Res.* **110**, 298–308 (2016).
40. Rachev, A. & Greenwald, S. E. Residual strains in conduit arteries. *J. Biomech.* **36**, 661–670 (2003).
41. Jadidi, M. et al. Mechanical, structural, and physiologic differences in human elastic and muscular arteries of different ages: Comparison of the descending thoracic aorta to the superficial femoral artery. *Acta Biomater.* **119**, 268–283 (2021).
42. Holzapfel, G. A. *Nonlinear Solid Mechanics: A Continuum Approach for Engineering* (Wiley, 2010).
43. Razian, S. A. & Jadidi, M. An optimized differential evolution algorithm for constitutive model fitting of arteries. *Acta Mech* **235**, 4149–4174 (2024).
44. Razian, S. A. & Jadidi, M. Histology Image Viewer and Converter (HIVC): A high-speed freeware software to view and convert whole slide histology images. *Comput. Methods Biomech. Biomed. Eng. Imag. Visual.* **11**(5), 1652–1660 (2023).
45. Chang, H. W. et al. Diameter and growth rate of the thoracic aorta—analysis based on serial computed tomography scans. *J. Thorac. Dis.* **12**, 4002–4013 (2020).
46. Mensel, B. et al. Thoracic and abdominal aortic diameters in a general population: MRI-based reference values and association with age and cardiovascular risk factors. *Eur. Radiol.* **26**, 969–978 (2016).
47. Kälsch, H. et al. Body-surface adjusted aortic reference diameters for improved identification of patients with thoracic aortic aneurysms: Results from the population-based Heinz Nixdorf Recall study. *Int. J. Cardiol.* **163**, 72–78 (2013).
48. Craiem, D. et al. Aging impact on thoracic aorta 3D morphometry in intermediate-risk subjects: Looking beyond coronary arteries with non-contrast cardiac CT. *Ann. Biomed. Eng.* **40**, 1028–1038 (2012).

49. Sokolis, D. P., Savva, G. D., Papadodima, S. A. & Kourkoulis, S. K. Regional distribution of circumferential residual strains in the human aorta according to age and gender. *J. Mech. Behav. Biomed. Mater.* **67**, 87–100 (2017).
50. Sokolis, D. P., Gouskou, N., Papadodima, S. A. & Kourkoulis, S. K. Layer-specific residual deformations and their variation along the human aorta. *J. Biomech. Eng.* **143**, 094504 (2021).
51. Zeinali-Davarani, S., Chow, M.-J., Turcotte, R. & Zhang, Y. Characterization of biaxial mechanical behavior of porcine aorta under gradual elastin degradation. *Ann. Biomed. Eng.* **41**, 1528–1538 (2013).
52. Chow, M.-J., Mondonedo, J. R., Johnson, V. M. & Zhang, Y. Progressive structural and biomechanical changes in elastin degraded aorta. *Biomech. Model Mechanobiol.* **12**, 361–372 (2013).
53. Collins, M. J., Eberth, J. F., Wilson, E. & Humphrey, J. D. Acute mechanical effects of elastase on the infrarenal mouse aorta: Implications for models of aneurysms. *J. Biomech.* **45**, 660–665 (2012).
54. Kim, J. et al. Crosslinked elastic fibers are necessary for low energy loss in the ascending aorta. *J. Biomech.* **61**, 199–207 (2017).
55. Shahbad, R., Kamenskiy, A., Razian, S. A., Jadidi, M. & Desyatova, A. Effects of age, elastin density, and glycosaminoglycan accumulation on the delamination strength of human thoracic and abdominal aortas. *Acta Biomater.* **189**, 413–426 (2024).
56. Humphrey, J. D. Possible mechanical roles of glycosaminoglycans in thoracic aortic dissection and associations with dysregulated transforming growth factor-β. *J Vasc Res* **50**, 1–10 (2013).
57. Ghadie, N. M., St-Pierre, J.-P. & Labrosse, M. R. Intramural distributions of GAGs and collagen versus opening angle of the intact porcine aortic wall. *Ann. Biomed. Eng.* **50**, 157–168 (2022).
58. Holzapfel, G. A., Gasser, T. C. & Ogden, R. W. A new constitutive framework for arterial wall mechanics and a comparative study of material models. in *Cardiovascular Soft Tissue Mechanics* (eds. Cowin, S. C. & Humphrey, J. D.) 1–48 (Kluwer Academic Publishers, Dordrecht, 2004). https://doi.org/10.1007/0-306-48389-0_1.
59. Ferruzzi, J., Vorp, D. A. & Humphrey, J. D. On constitutive descriptors of the biaxial mechanical behaviour of human abdominal aorta and aneurysms. *J. R. Soc. Interface* **8**, 435–450 (2011).
60. Kazim, M. et al. Variability in structure, morphology, and mechanical properties of the descending thoracic and infrarenal aorta around their circumference. *J. Mech. Behav. Biomed. Mater.* **150**, 106332 (2024).
61. Blacher, J. & Safar, M. E. Large-artery stiffness, hypertension and cardiovascular risk in older patients. *Nat. Rev. Cardiol.* **2**, 450–455 (2005).
62. Jadidi, M. et al. Calcification prevalence in different vascular zones and its association with demographics, risk factors, and morphometry. *Am. J. Physiol. - Heart Circ. Physiol.* **320**, H2313–H2323 (2021).
63. Seyedsalehi, S., Zhang, L., Choi, J. & Baek, S. Prior distributions of material parameters for bayesian calibration of growth and remodeling computational model of abdominal aortic wall. *J. Biomech. Eng.* **137**, 101001 (2015).
64. Díaz, C., Peña, J. A., Martínez, M. A. & Peña, E. Unraveling the multilayer mechanical response of aorta using layer-specific residual stresses and experimental properties. *J. Mech. Behav. Biomed. Mater.* **113**, 104070 (2021).

Acknowledgements

We wish to acknowledge Live On Nebraska for their help and support in collecting the blood vessels and thank donors and their families for making this study possible. We also thank the Tissue Analysis Core (TAC) at the Center for Cardiovascular Research in Biomechanics (CRiB) for their help and support. This work was partly supported by the National Heart, Lung, And Blood Institute (NHLBI) of the National Institutes of Health (NIH) under the Award Number R01HL147128, the National Institute of General Medical Sciences (NIGMS) under the Award Number P20GM152301, and the Nebraska Tobacco Settlement Biomedical Research Development Fund.

Author contributions

R.S. contributed to Data Collection, Analysis and Interpretation, Visualization, and Writing and Manuscript Preparation. M.K. contributed to Data Collection, Analysis and Interpretation, and Writing and Manuscript Preparation. S.R. contributed to Data Analysis and Interpretation, and Writing and Manuscript Preparation. A.D. contributed to Critical Review, Resources, Funding Acquisition, and Conceptualization and Study Design. M.J. contributed to Conceptualization and Study Design, Data Analysis and Interpretation, Writing and Manuscript Preparation, Supervision and Leadership, and Funding Acquisition. All authors reviewed and approved the final manuscript.

Competing interests

The authors declare no competing interests.

Ethics approval

The human aortic tissues used in this study were obtained from deceased donors through an organ procurement organization (Live On Nebraska) with informed consent provided by the next of kin. The collection and use of these tissues adhered to all relevant guidelines and regulations, including the Declaration of Helsinki. According to the U.S. Department of Health and Human Services and institutional guidelines, research involving cadaveric tissues does not constitute research on human subjects and, therefore, does not require Institutional Review Board (IRB) approval. Ethical approval was waived due to the nature of the study. All experiments were conducted in accordance with IBC protocol #20-10-045-BL2, which was approved by the University of Nebraska at Omaha Environmental Health and Safety Office.

Additional information

Supplementary Information The online version contains supplementary material available at https://doi.org/10.1038/s41598-025-95008-8.

Correspondence and requests for materials should be addressed to M.J.